Nanoscale

Accepted Manuscript

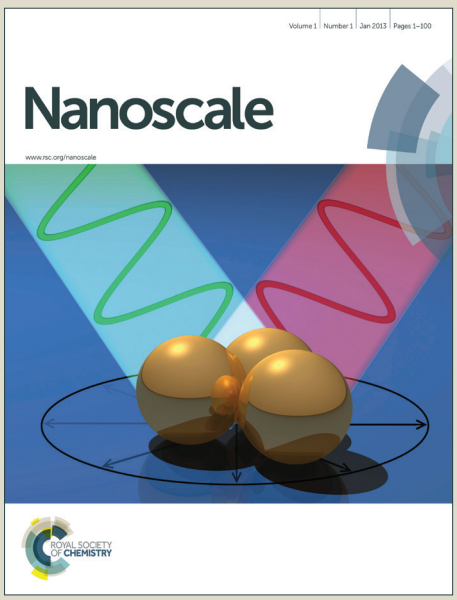

ROYAL SOCIETY OF CHEMISTRY

www.rsc.org/nanoscale

Journal Name

RSCPublishing

ARTICLE

Size-Controlled SnO_2 Hollow Spheres via Template Free Approach as Anodes for Lithium Ion Batteries

Cite this: DOI: 10.1039/x0xx00000x

Akkisetty Bhaskar,[a] Melepurath Deepa[b] and Tata Narasinga Rao[c]

Received 00th January 2012,
Accepted 00th January 2012

DOI: 10.1039/x0xx00000x

www.rsc.org/

Tin oxide hollow spheres (SnO_2 HS) with high structural integrity were synthesized by using a one pot hydrothermal approach with organic moieties as structure controlling agents. By adjusting the proportion of acetylacetone (AcAc) in the precursor formulation, SnO_2 HS of 200 and 350 nm dimensions, with uniform shell thicknesses of about 50 nm were prepared. Using the optimized solution composition with a Sn precursor, a heating duration dependent structural evolution of SnO_2 performed at a fixed temperature of 160 ^oC, revealed a transition from solid spheres (1 h) to aggregated spheres (4 h) to porous spheres (10 h) to optimized HS (13 h) and finally to broken enlarged HS (24 h). A heating temperature dependent study carried out with a constant heating span of 13 h showed a metamorphosis from spheres with solid cores (140 ^oC) to ones with hollow cores (160 ^oC), culminating with fragmented HS, expanded in dimensions (180 ^oC). A growth mechanism was proposed for the optimized SnO_2 HS (2.5 or 5.0 mL of AcAc, 160 ^oC, 13 h) and the performance of these HS as anodes for Li ions batteries was evaluated by electrochemical studies. The 200 nm SnO_2 HS demonstrated an initial lithium storage capacity of 1055 mAh g^{-1} at a current density of 100 mA g^{-1}, and it retained a capacity of 540 mAh g^{-1} after 50 charge-discharge cycles. The SnO_2 HS also showed excellent rate capability as the electrode exhibited a capacity of of 422 mAh g^{-1} even at a high current density of 2000 mA g^{-1}. The notable capacity of SnO_2 HS is a manifestation of the mono-disperse quality of the SnO_2 HS coupled with the high number of electrochemically addressable sites, afforded by the large surface area of the HS and the striking cyclability is also attributed to the unique structure of HS, which is resistant to degradation upon repeated ion insertion/extraction. The SnO_2 HS were also found to be luminescent, thus indicating their usefulness for not only energy storage but also for energy harvesting applications.

Introduction

Hollow structures of transition metal oxides have generated significant research interest for they are employable as electrodes in a wide spectrum of applications such as lithium ion batteries, chemical sensors, photovoltaic cells and supercapacitors.[1-5] The development of novel anode materials capable of delivering high energy density and cycling stability as alternates to traditional graphite electrode continues to be an arduous challenge in lithium ion battery (LiB) research, which is addressed to some extent by use of hollow structures. Typical attributes of hollow structures like nanospheres with empty interiors include: a large surface to volume ratio, low density, short solid-state diffusion lengths and a low thermal expansion coefficient. These features in particular, render them suitable as anodes for next generation LiBs. Among various oxides like MoO_2, SnO_2, TiO_2, F_3O_4, Co_3O_4, V_2O_5 and so forth,[6-9] Sn based anode materials are promising, owing to a high theoretical specific capacity (782 mA h g^{-1} for SnO_2 and 990 mAh g^{-1} for Sn), relative ease of synthesis in the form of hollow structures, low cost and a high average Li-ion intercalation potential (~ 0.5 V).[10,11] The practical usage of SnO_2 is based on Li metal alloying/de-alloying reactions, which involve an initial irreversible transformation of SnO_2 to Sn followed by a reversible alloying with Li metal to form a $Li_{4.4}Sn$ alloy.[11] The reversible alloying reaction is accompanied by an almost 300% increase in volume and upon repeated cycling, the SnO_2 active electrode can undergo pulverization which causes breakdown in electrical contact pathways between adjacent particles, leading to rapid capacity decline.[12-14] In order to alleviate the pulverization problem of SnO_2-based anodes, nanosized SnO_2 have been commonly employed to reduce the volume change that occurs during the charge and discharge cycles.[14-17] However, SnO_2 nanoparticles tend to aggregate after several reaction cycles due to their high surface energy, and thus their size advantages are lost. To address this issue, complex

nanostructures of SnO_2 such as hollow spheres, core/shells, nanowires, nanoflowers, nanotubes, nanosheets have been developed in the past[18-34] as in nanosized SnO_2, the volume change caused by the mechanical stress induced by lithium intercalation is tolerated more easily than it is in bulk SnO_2. Hollow structures, in particular, can partially accommodate the large volume change, delaying capacity fading.

Various synthetic strategies have been used to prepare spherical hollow nanostructured materials; among them the most common approach is the template-assisted synthesis.[24-27] Typically, in this method the templates that are used should be prepared in advance and later they are washed away. The products morphology can be controlled through the selection of the appropriate templates. However, there are some limitations using this method that restrict the large scale application. It is difficult to prepare suitable templates; in general the template removal process may lead to hollow structures destruction. Moreover, the template preparation processes are usually complex, time consuming and costly. As a result, several new routes for generating hollow nanostructures have been explored by employing different mechanisms, including nanoscale Kirkindal effect, oriented attachment and Ostwald ripening.[36-39,22] The formation of hollow nanostructures via an Ostwald ripening mechanism is generally accomplished using solvothermal methods. For example, Lou et al. prepared SnO_2 hollow nanostructures based on an inward-out Ostwald ripening mechanism. The synthesis was performed in an ethanol–water mixed solvent using potassium stannate as the precursor. The hollow nanostructure showed a very high initial capacity 1140 mAh g^{-1}.[22] Wang et al. prepared hierarchical SnO_2 solid and hollow microspheres in water via a simple hydrothermal method, using tin (IV) chloride pentahydrate as the tin source and NH_4F or NaF as the morphology controlling agents. The hierarchical SnO_2 hollow spheres retained a discharge capacity from 1465 to 187 mAh g^{-1} after 50 cycles.[23] Although appreciable progress in the template-free fabrication of hollow nanostructures has been achieved in the past, the control of size and performance continues to be a daunting challenge.

Here we present a template-free, one-pot hydrothermal approach for preparing SnO_2 HS with controlled HS size by using organic additives as structure directing agents. The role of the proportion of the organic moiety, namely, acetylacetone (AcAc) and the thermal conditions which steer the growth of SnO_2 HS with an optimum size for efficient electrochemical energy storage performance, has been followed by field emission scanning electron microscopy (FESEM) and high resolution transmission electron microscopy (HRTEM). By tuning the processing parameters, SnO_2 HS with a narrow size distribution and good structural integrity were prepared. The optimization of SnO_2 HS (size and empty core dimensions) has been accomplished by evaluating the Li ion storage performance of various electrodes. In addition, the SnO_2 HS were also found to be luminescent, indicating a dual function capability, as the blue light emitting property can be of use in applications which require both energy storage and emission.

Experimental

SnO_2 hollow spheres (HS) and nanostructures

Hollow spheres of SnO_2 were prepared by a one-step hydrothermal synthesis route using water as solvent. Typically, 1 mL of acetylacetone (AcAc, Aldrich, 98%) was taken in a 100 mL beaker and to this solution 3.324 mmol of $SnCl_2.2H_2O$ (Merck, 98%) was added and stirred for 5 min. To the resulting clear solution, 40 mL of ultrapure water and 1.1 g of 3-mercapto propionic acid (MPA, Alfa Aesar, 98%) was added and stirred for 30 min. To the resulting solution, 100 mg of cetyltrimethylammoniumbromide (CTAB, Alfa Aesar, 98%) surfactant followed by 10 ml of ultrapure water were added and stirred for 1 h. The resulting solution was transferred to a 80 mL Teflon lined stainless steel autoclave. After heating at 160 °C for 13 h in an oven, the resulting pale yellow color precipitate was filtered and washed with water and dried at 80 °C for 6 h. Similarly, three more precursor solutions with 2.5 mL, 5 mL and 10 mL of AcAc were also prepared while maintaining all other concentrations constant. These solutions were also subjected to the 160 °C for 13 h heat treatment in an autoclave and the three products obtained were analyzed and compared with the one obtained using 1 mL AcAc. The effect of temperature on the morphology of the samples obtained from the solution prepared with 5 mL of AcAc while keeping other concentrations same was studied by heating this solution at two more temperatures of 140 and 180 °C. Solution with precursors 3.3 mmol $SnCl_2$. $2H_2O$, 5 mL of AcAc and 100 mg CTAB but without any MPA and yet another precursor solution with 3.3mmol $SnCl_2$. H_2O, 1.1 g of MPA and 5 mL of AcAc without adding any CTAB were also prepared. These two solutions (without MPA and without CTAB respectively) were subjected to the 160 °C, 13 h heat treatment in an autoclave to obtain SnO_2 products.

Electrodes Preparation

Working electrodes were prepared by mixing 80 wt. % of active material (SnO_2), 10 wt. % acetylene black and 10 wt. % polyvinylidene fluoride with a few drops of N-methyl pyrrolidine. The resultant slurry was coated on 13 mm stainless steel foils and dried at 80 °C for 4 h in vacuum oven for removing the solvent. Swagelok cells were employed for electrochemical measurements and these were assembled inside an argon filled glove-box (O_2 and H_2O concentration $\leq$ 0.5 ppm and 0.5 ppm, respectively). A lithium foil was used as a counter/reference electrode and a Whatman glass microfiber filter paper functioned as the separator. The electrolyte was 1 M $LiPF_6$ dissolved in a mixture of ethylene carbonate (EC) and dimethyl carbonate (DMC) (1:1 v/v).

Characterization techniques

Galvanostatic charge-discharge measurements were performed on a battery testing unit (Arbin Instruments, BT 2000) at different current densities in the range of 0.01 – 2 V *versus* Li/Li^+ at room temperature. Cyclic voltammetry (CV) and electrochemical impedance spectroscopy (EIS) measurements on the electrodes were performed on an Autolab PGSTAT 302N coupled with NOVA software. X-ray diffraction on the electrodes was performed on a PANalytical, X'PertPRO instrument using Cu K_α of 1.5406 Å wavelength.

Structural characterization was carried out by HRTEM (JEOL 3010 200 KV). For HRTEM, the sample was ultrasonicated for 0.5 h and carefully extracted onto a carbon coated copper grid. Brunauer-Emmett-Teller (BET) specific surface area measurement on samples was performed on a Micromeritics, ASAP 2020. UV-Visible spectra measurement was performed on Shimadzu, UV-3600. Photoluminescence property was carried out on Horiba, Fluoromax-4.

Results and discussion

Structural aspects

Powder X-ray diffraction (XRD) patterns of SnO_2 samples prepared from precursor solutions containing 1, 2.5, 5 and 10 mL of AcAc are shown in Figure 1. The XRD pattern of the sample prepared from a solution containing 1 mL of AcAc matches well with the standard diffraction pattern of SnO_2 with a tetragonal crystal structure however extraneous peaks from SnS (impurity) were also observed (JCPDF # 75-2115). The diffraction peaks corresponding to SnO_2 prepared from solutions with 2.5, 5 and 10 mL of AcAc are assigned to the tetragonal crystal structure of SnO_2 with space group $P4_2/mnm(136)$ (JCPDF # 77-0447). In these three samples, no characteristic peaks corresponding to impurities such as SnS or SnS_2 were observed, thus confirming that pure phase SnO_2 was formed successfully from solutions with higher proportion of AcAc. Further a systematic increase in FWHM of the main diffraction peaks of SnO_2 was observed as a function of increasing AcAc content. After annealing, the sample prepared from a solution encompassing 5 mL AcAc at 500 °C for 3 h air, the XRD pattern of the resulting sample was compared with that of the as-prepared sample. The as-prepared sample showed broader peaks compared to the annealed sample, thus illustrating that annealing increases the crystallite size of SnO_2. The diffraction patterns of the as-prepared sample (solution prepared from 5 mL AcAc autoclaved at 160 °C for 13 h) were down shifted compared to the annealed sample by $2\theta = 0.1°$. This is clearly visible from the enlarged view of the high intensity peak plotted for the as-prepared and annealed samples (Figure S1, supporting information). Oxygen deficiency in the as-prepared sample leading to slightly sub-stoichiometric SnO_{2-x} could be one reason for this downshift.

Optical characteristics

To confirm oxygen deficiency in the as-prepared SnO_2 HS (prepared from a solution with 5 mL AcAc and 160 °C hydrothermal treatment for 13 h) the UV-Visible spectra of as-prepared SnO_2 HS and annealed SnO_2 HS (500 °C for 3 h) were recorded (Figure 2a) in diffuse reflectance mode and converted to absorbance. The optical band gaps for the two samples were calculated from their absorption edges. The optical transitions in crystalline SnO_2 are direct.[40] The as-prepared and annealed samples of SnO_2 HS show band gaps of 3.2 and 3.44 eV, respectively. The annealed SnO_2 HS shows a band gap close to that of bulk (commercial) SnO_2 ($E_g = 3.6$ eV). The lowering of band gap in the as-prepared HS could be due to the presence of a oxygen vacancies to form sub-stoichiometric SnO_{2-x} HS, upon annealing a stoichiometric SnO_2 will has been obtained.

Figure 2b shows the comparative room temperature photoluminescence emission spectra of as-prepared (prepared from a solution with 5 mL AcAc and 160 °C hydrothermal treatment for 13 h) and annealed SnO_2 HS, recorded at an excitation wavelength of 325 nm. The emission was measured in the wavelength range of 400 to 630 nm. Both as-prepared and annealed SnO_2 HS samples show three peaks at 443, 468 and 535 nm. The broad peak centered at 443 nm was observed earlier for a SnO_2 nanoblades array by Her et al.[41] and the peak at 468 nm was also observed for SnO_2 nano flowers by Wang et al.[42] Since the position of these emission maxima are lower than the respective band gaps of the SnO_2, these emission cannot be attributed to the direct recombination of conduction band electrons in the Sn4p band and the holes in the O2p valence band. Therefore, these bands can be assigned to oxygen-related defects introduced during hydrothermal growth. The interactions between oxygen vacancies and the interfacial tin vacancies lead to the formation of a significant number of trapped states, which form a series of metastable energy levels within the band gap and result in an emission in the low energy region. Apart from these three peaks, the as prepared SnO_2 HS shows two more weak peaks centered at 562 and 622 nm. The origin of these two peaks might be correlated to a greater defect concentration, compared to the annealed SnO_{2-x} HS.

Electron microscopy analyses

Morphological studies of the samples prepared with various amounts of AcAc have been performed using FE-SEM and the images are shown in Figure 3. The FE-SEM image of the sample prepared from a solution with 1 mL of AcAc shows (Figure 3a) aggregated spherical particles of SnO_2. When the amount of AcAc was increased to 2.5 and 5 mL, the FE-SEM images of both the samples show spherical particles of SnO_2 are in the range of 250 - 400 and 450 - 750 nm dimensions, respectively (Figure 3b and c). Some broken spheres with cavities are visible in the images of both samples, further demonstrating the hollow nature of the products. The FE-SEM images after incorporating 10 mL of AcAc shows the formation of aggregated SnO_2 hollow spheres with a wide distribution in size (Figure 3d).

In order to confirm the hollow nature and the size of the spheres, HRTEM was performed on SnO_2 HS prepared from solutions containing 2.5 and 5 mL of AcAc. The HRTEM image (Figure 4a) of SnO_2 HS prepared from a solution with 2.5 mL AcAc, shows a sharp contrast (dark/bright) between the boundary and the center of the spheres, thus confirming their hollow nature. The size of these SnO_2 HS is in the range of 200-300 nm and the shell thickness of each hollow sphere is ~50 nm. Distinct lattice fringes are observed in the Figure 4b of the hollow sphere which show that each sphere is composed of small crystallites of about ~ 8 nm dimensions and the fringe separation of 0.33 nm matches very well with the (110) plane of the tetragonal crystal structure of SnO_2. The TEM image of sample prepared from a solution with 5 mL of AcAc shows (Figure 4c) the hollow nanostructure of SnO_2 with an outer diameter in the range of 350-400 nm and the shell thickness is approximately 60 nm. Figure 4d shows that each hollow sphere

is constituted by SnO_2 crystallites of ~7 nm dimensions and the inter-fringe distance of 0.33 nm confirms the tetragonal crystal structure of SnO_2 HS. Our HRTEM results concur with our XRD findings.

Growth mechanism

To explain the SnO_2 HS formation mechanism, time dependent experiments were performed by hydrothermally heating the precursor solution containing 3.3 mmol of $SnCl_2.2H_2O$, 5 mL of AcAc, 1.1 g of MPA and 100 mg CTAB for intervals of 1, 4, 10, 13 and 24 h at a constant temperature of 160 °C. XRD patterns and TEM images were collected at the end of each interval and these are shown in Figure S2 (supporting information) and 5. The corresponding SEM images are shown in Figure S3. The XRD pattern of sample obtained after heating for 1 h shows an amorphous nature whereas after heating for 4, 10, 13 and 24 h, each of the ensuing samples shows diffraction peaks corresponding to the tetragonal crystal structure of SnO_2 (JCPDF # 77-0447) and no other impurity peaks were observed. The TEM images of the products obtained at the initial stage i.e., after 1 h heat treatment shows (Figure 5a) solid spheres with solid cores and smooth exterior surfaces which are almost amorphous (inferred from XRD pattern) and the average diameter is about 330 nm. After prolonging the duration to 4 h, the TEM image of the product shows spherical particles (Figure 5b). Since XRD revealed SnO_2, to be crystalline, at this point, some of the spheres tend to undergo aggregation, to acquire crystalline structures, which are thermodynamically more stable. The dark contrast in the spheres indicates that the spheres are not hollow at this juncture and spheres continue to retain their solid cores. Upon increasing the heating duration to 10 h, the morphology of the product undergoes a dramatic transformation, in terms of sphere core content. The corresponding image shows loosely packed discrete spheres, with a non-uniform size distribution, and there are empty spaces clearly seen in the cores of the spheres (Figure 5c). Figure 5d shows the image of a single sphere (10 h), the periphery of the sphere is rough and pores can be detected (encircled by dashed lines), which indicates that evacuation starts at this stage and the size of the SnO_2 hollow spheres is in the range of 80 to 400 nm (Figure S3c). The wide distribution in the sphere size is clearly evident in Figure S4. As heating is continued, the core of the sphere dissolves and re-deposits on the outer surface of the shell which results in an increase in sphere size. Further, when the heating duration was increased to 13 h, the structure consolidates, as hollow spheres of SnO_2 with solid shells were obtained (Figure 5e), the shell thickness is almost uniform and the outer diameters of the spheres are also similar, indicating that this heating duration is optimum for producing mono-dispersed SnO_2 HS. The average sphere size is about 350 nm. After heating for 24 h, the product morphology continues to comprise (Figure 5f) of spherical HS but the diameter of the spheres increases to about 750 nm with a shell thickness of ~100 nm. The increase in sphere size is consistent with an increasing degree of crystallinity which causes grain coarsening. When the solution is heated for 24 h, the HS undergo self-expansion, but not at the expense of the evacuated cores, for the HS structure is retained, albeit a few fractured HS, due to the stresses engendered upon HS enlargement. This also complies with the corresponding FE-SEM image (Figure S3e, Supporting information) wherein sphere size increment along with an increasing proportion of broken hollow spheres were observed.

Initially, when $SnCl_2$ precursor was added to AcAc and stirred for 5 min, it forms a clear solution of $Sn(AcAc)_2Cl_2$ complex[43] and when the solution was continuously stirred for 1 h, a colloidal suspension was obtained. Further addition of 40 mL water and 1 mL of MPA, and stirring resulted in the formation of a clear solution owing to a stronger complexing ability of MPA[44] compared to AcAc, whereby AcAc moieties around Sn are completely replaced by MPA to result in a clear sol. The $Sn(AcAc)_2Cl_2$ is thus transformed to a Sn(MPA) complex. Subsequent addition of CTAB, followed by hydrothermal heat treatment causes the decomposition of the Sn(MPA) complex and SnO_2 is formed. All the above steps have been shown below through equations.

$$SnCl_2.2H_2O + O_2 + 2CH_3COCH_3CO \rightarrow Sn(OCCH_3COCH_3)_2Cl_2 \quad (1)$$

$$Sn(OCCH_3COCH_3)_2Cl_2 + HSCH_2CH_2COOH \rightarrow Sn(SCH_2CH_2COOH)_2 + CH_3COCH_3CO + HCl \quad (2)$$

$$Sn(SCH_2CH_2COOH)_2 \rightarrow SnO_2 \quad (3)$$

On the basis of XRD and TEM observations of the samples subjected to the time dependent study, we propose an inward out Ostwald ripening mechanism for the formation of SnO_2 hollow spheres. Initially after heating hydrothermally for 1 h, solid (amorphous) spheres of SnO_2 with dimensions of about 330 nm were formed and they remain spheres with solid cores, even after a 4 h hydrothermal heating treatment. When the heating duration was prolonged to 10 h, porous spherical nanostructures comprising of ultra-fine particles which are loosely packed in the interior and tightly packed along the outer surface were formed. When the heating duration was raised to 13 h, the outer surface of sphere which is in direct contact with the solution grows due to Ostwald ripening. Because of a very high interfacial energy of loosely packed small crystallites in the interior of the spheres, and in order to minimize the total energy of the system, the interior particles dissolve and redeposit on the outer surface. As a result, hollow spherical structures are formed. Further when the heating duration was increased to 24 h, more and more interior part of the spheres dissolve and recrystallize on the outer surface and the spheres expand and after 24 h, the size of the hollow sphere is around 750 nm. Furthermore, owing to the large size of the HS at this point, many of them break open due to mechanical stress generated by sphere expansion.

The roles of synthetic parameters like effect of temperature, key roles of MPA, CTAB and AcAc for the formation of SnO_2 hollow spheres was analysed systematically. The effect of temperature for the formation of SnO_2 HS was studied by examining samples prepared from solutions with 3.3 mmol of $SnCl_2.2H_2O$, 5 mL of AcAc, 1.1 g MPA and 100 mg CTAB, followed by hydrothermal heating at 140 and 180 °C for 13 h. The FE-SEM image of the sample prepared at 140 ^oC shows a

mono-disperse solid spheres of the size of about 500 nm. The solid core of the solid sphere was also confirmed with the TEM image which is shown in the inset of Figure 6a. The FE-SEM image of the SnO_2 synthesized at 180 °C (for 13 h) shows hollow spheres of SnO_2 with outer diameter ~ 800 nm (Figure 6b). It can also be seen from FE-SEM most of the HS were broken at this higher temperature. It is evident that the hydrothermal treatment at 160 ^oC for 13 h leads to SnO_2 HS with optimum dimensions and structural integrity. The roles of CTAB and MPA in the formation of SnO_2 hollow spheres were determined by preparing the SnO_2 with the solution containing 3.3 mmol of $SnCl_2.2H_2O$, 5 ml of AcAc and MPA (no CTAB) as well as the solution with 3.3 mmol of $SnCl_2.2H_2O$, 5 ml of AcAc and CTAB (no MPA). In both the cases, the solution was heated at 160 °C for 13 h. The FE-SEM image of SnO_2 prepared from a solution with no CTAB shows (Figure 6c) aggregated spheres with thick shells whereas the micrograph of SnO_2 obtained from the solution with no MPA reveals (Figure 6d) the formation of flaky particles of irregular shapes and sizes. The FE-SEM images and analyses for SnO_2 samples prepared from only MPA, only CTAB and only CTAB+MPA (1:3 mol ratio) (Figure S5), confirmed that AcAc helps in the formation of SnO_2 devoid of any SnS.

From FE-SEM analyses, we found that from the group of the three reagents: MPA, CTAB and AcAc, when any two or any one of the three was used for preparing the Sn salt precursor solution and then, SnO_2 by 13 h hydrothermal heating at 160 ^oC, mono-disperse non-aggregated SnO_2 HS were not formed. Only when the three reagents were incorporated in the Sn salt solution, discrete SnO_2 HS were obtained. Since from all MPA based solutions (with CTAB or AcAc or without them), spherical structures were obtained, it was concluded that MPA is the structure directing agent. Further, from the hard and soft acid-base concept, the alkylcarboxylate in MPA can serve as a hard base, and will have a strong affinity for acidic Sn^{4+} species. The MPA molecules can easily form a monolayer around Sn^{4+} species in a manner similar to the way they attach to TiO_2[45] and therefore this binding might be steering the growth of spherical shapes. Scheme 1 shows the formation of SnO_2 HS, by use of the three reagents. During hydrothermal heating, the Sn^{4+} species is capped by MPA, decomposes to form primary particles of SnO_2 (amorphous) which can aggregate to form bigger spherical particles at the end of 1 h heating. This is stage very critical for the formation of SnO_2 HS. Oxygen from the MPA caps the Sn^{4+} in SnO_2, and CTAB, being a cationic surfactant will have a propensity to associate with oxygens on SnO_2 and prevents the aggregation of particles. The organic moieties (MPA) and surfactant CTAB possibly induce recrystallization on the surface of SnO_2 sphere and the inner particles of the sphere remain largely unaffected. Further, when the heating duration was increased to 10 h, the outer particles coarsen and the inner particles dissolve, due to their high interfacial energy. After 13 h, mono-disperse hollow spheres with well-defined shells were formed. The action of AcAc is not very clear, for when SnO_2 was prepared from a CTAB/MPA/Sn^{2+} solution, (devoid of AcAc), while SnO_2 HS were obtained, but SnS phase was also detected, and the latter was found to be non-existent when AcAc (2.5, 5 and 10 mL) was also added to the CTAB/MPA/Sn^{2+} solution. Microstructural analyses clearly shows that MPA is responsible for the formation of spherical shapes, CTAB assists in maintaining the HS as discrete entities with distinct grain boundaries and AcAc ensures a pure phase (only SnO_2).

Surface area determination

The Brunauer-Emmet-Teller (BET) specific surface area and pore size distributions of the 200, 350 and 750 nm SnO_2 HS were characterized by nitrogen adsorption-desorption isotherm measurements and are shown in Figure 7a, b and c, respectively. From Figure 7 the BET surface areas for the 200, 350 and 750 nm SnO_2 HS were determined as 72.3, 86.6 and 41.3 $m^2\ g^{-1}$. The hysteresis loops and pore size distribution curves which are shown in the insets of Figure 7 imply a typical mesoporous nature for all the three 200, 350 and 750 nm SnO_2 HS. The average sizes of the mesopores calculated from the insets of Figure 7 were: 5 nm for the 200 nm HS (Figure 7a), 4.5 nm for the 350 nm HS (Figure 7b) and 5.7 nm for the 750 nm HS (Figure 7c). The very high specific surface area and the mesoporosity of HS indicates that a very high capacity can be expected for these three materials when used as Li-ion battery anodes.

Electrochemical Li storage behavior

The lithium storage properties of SnO_2 HS as anodes for Li-ion batteries was evaluated using a two electrode cell, where SnO_2 HS served as the working electrode and Li metal as reference and counter electrodes. The effects of the SnO_2 HS size on the electrochemical performance are compared. Figure 8a shows the cyclability comparison of 200, 350 and 750 nm SnO_2 HS measured in the voltage range of 0.01-2 V at a constant current density of 100 mA g^{-1}. The three samples; 200, 350 and 750 nm SnO_2 HS exhibit initial reversible capacities of 1055, 854.5 and 970 mAh g^{-1}, respectively. The capacities of all the three electrodes fade gradually with cycling. Among the three samples, the 200 nm size SnO_2 HS showed a good cyclability as it retained a capacity of 540 mAh g^{-1} after 50 cycles whereas the 350 and 750 nm SnO_2 HS retained capacities of 350 and 200 mAh g^{-1} at the end of 50 cycles. The typical charge-discharge profiles for the SnO_2 HS of size around 200 nm for the initial three cycles are shown in Figure 8b. From the charge-discharge profiles it can be seen that the initial discharge and charge specific capacities are 2242.4 and 1055 mAh g^{-1}, respectively with a Coulombic efficiency of around 47 %. There are three possible reasons that contribute the large irreversible capacity loss during the first discharge cycle; (i) from the decomposition of electrolyte and the formation of solid electrolyte interface (SEI) layer on the surface of electrode. (ii) the irreversible conversion reaction of SnO_2 to Sn and Li_2O and, (iii) from the interfacial storage of excess lithium ions between Sn nanoparticles and Li_2O.[46] The SEI layer formation and alloying/dealloying potentials were measured by recording cyclic voltammograms (CVs). Figure 8c

shows the CV curves for the SnO_2 HS (of 200 nm in Size) electrodes performed at a scan rate of 0.1 mV s^{-1} during the first five cycles. The CV curves are consistent with the literature confirming the following electrochemical reaction pathway. During the first cathodic scan three reduction peaks were observed. An irreversible peak observed at 1.3 V corresponds to SEI layer formation[26] and a broad peak at ~ 1 V is ascribed to the conversion reaction of SnO_2 to Sn and Li_2O. The third prominent peak in the voltage range 0.6 to 0 V corresponds to $Li_{4.4}Sn$ alloy formation reaction. Similarly during the first anodic scan two distinct peaks were observed. The peak between 0.3 to 0.8 V is due to $Li_{4.4}Sn$ to Sn dealloying reaction and a broad peak at ~ 1.2 V is attributed to the partial oxidation reaction of Sn to SnO on the surface of the electrode. The alloying/dealloying reaction redox peaks decline slowly as a function of increasing number of cycles whereas the SnO_2/Sn conversion peak decays rapidly. This suggests that the alloying/dealloying process is highly reversible. The electrochemical storage mechanism can be written as follows:

$$SnO_2 + 4Li^+ + 4e^- \rightarrow Sn + 2Li_2O \quad (4)$$

$$Sn + xLi^+ + xe^- \leftrightarrow Li_xSn \quad (0 \leq x \leq 4.4) \quad (5)$$

Figure 8d shows the rate capabilities of SnO_2 HS of three different sizes, measured at different current densities. Among all the three samples, the 200 nm SnO_2 HS exhibited an excellent rate capability. Even at a very high current density of 2000 mA g^{-1}, the electrode showed a capacity of 422 mAh g^{-1} whereas at the same current density, the 350 and 750 nm SnO_2 HS showed capacities of 368 and 233 mAh g^{-1} respectively. At the end of 30 cycles and at a current density 100 mA g^{-1}, the 200 nm SnO_2 HS retained a capacity of 656 mAh g^{-1} and notably this was achieved after several charge-discharge cycles at various current densities. The very high capacity and good rate capability of the 200 nm SnO_2 HS is due to very high surface area and optimum mesopore size. As the sphere size of SnO_2 HS decreases, we observed superior electrochemical performance, as small sized particles can tolerate the volume expansion more easily than large particles. The as-fabricated cell shows a V_{OC} of ~ 3 V, and the cell was discharged to 0.01 V, prior to measuring the capacity *versus* cycling response over a potential window confined to 0.01 to 1 V. Noticeably, when the charge-discharge characteristics of 200 nm size SnO_2 HS were measured in the voltage range of 0.01 to 1 V at a constant current density of 100 mA g^{-1}, a stable cycle performance was achieved for 50 cycles (Figure 9a). The reversible capacity decreased from 637.3 mAh g^{-1} (for 5th cycle) to 513 mAh g^{-1} (for 50th cycle). The increased cycling stability when cycled within a voltage window of 0.01–1 V is due to the prevention of the surface reaction between Sn and Li_2O which occurs at higher voltages and also due to the minimization of solid electrolyte interface (SEI) formation on Sn. The average sizes of the mesopores calculated from the insets of Figure 7 were: 5 nm for the 200 nm HS (Figure 7a), 4.5 nm for the 350 nm HS (Figure 7b) and 5.7 nm for the 750 nm HS (Figure 7c) of SnO_2. The Li-ion charge storage mechanism not only depends on the surface area but also pore size and inner void space. We define "pores" as the inter-crystallite and inter-particle separations and "voids" as the diameter of the inner hollow sphere. Larger the pore size and void space, more easily it can access Li^+ ions, during charge-discharge. Among the three different sizes of the spheres, the pore size and inner void space for 750 nm SnO_2 HS are larger and hence there would be an increase in specific charge storage capacity during the initial few cycles. However, the long term cycling response is superior for the 350 nm HS compared to the 750 nm HS, as the smaller sized spheres accommodate the volume change without breaking as opposed to the larger spheres which can break upon repeated Li^+ intercalation and deintercalation.

The increased cycling stability was further validated by measuring electrochemical impedance spectra (EIS). Figure 9b shows the comparison of the EIS plots of 200 nm SnO_2 HS measured after 50 charge-discharge cycles performed between 0.01-1V and 0.01-2 V. The Nyquist plots show one semicircle followed by an inclined straight line; the latter is ascribed to the low frequency region. The semicircle is assigned to a parallel combination of charge transfer resistance (R_{CT}) and electrical double layer capacitance (C_{dl}), and the straight line originates from the diffusion of charged species through the bulk of the electrode material. From the Nyquist plots it can be observed that after 50 cycles the R_{CT} for the charge-discharge cycles measured in the voltage range 0.01-1 V is much lesser than the R_{CT} obtained between 0.01-2 V, indicating that when the upper cut of voltage is restricted to 1 V the charge transfer process between electrode and electrolyte is more facile that at 2 V. This could be due to minimization of surface reaction of Sn and Li_2O and the side reactions between electrode and electrolyte.

Conclusions

A simple hydrothermal method was employed for preparing SnO_2 HS, with the aid of organic moieties as structure directing agents. The content of AcAc in the Sn precursor dispersion was found to have a direct impact on the structure of the final SnO_2 product. Uniform SnO_2 HS with overall diameters of 200 and 350 nm comprising of empty cores surrounded by solid shells of 50 to 60 nm dimensions were successfully prepared from solutions with 2.5/5.0 mL of AcAc. A heating time dependent analyses delineated a stepwise transformation of solid spheres (1 h) to agglomerated spheres (4 h) to porous spheres (10 h) to optimized HS (13 h) terminating with broken blown-up HS (24 h). A temperature dependent reaction progress showed conversion from solid spheres (140 ^oC) to HS (160 ^oC) to chipped off-huge spheres (180 ^oC). The roles of MPA as the sphere forming agent, CTAB as the surfactant which inhibits clumping of SnO_2 HS and AcAc, as the moiety responsible for pure phase formation were also deduced. On the basis of morphological analyses, a growth mechanism for the formation of optimized SnO_2 HS was expounded. The ability of the optimized SnO_2 HS (2.5 or 5.0 mL of AcAc, 160 ^oC, 13 h) to function as anodes in lithium ion batteries was determined from their electrochemical characteristics. The 200 nm SnO_2 HS delivered a reversible capacity of 540 mAh g^{-1} at a current density of 100 mA g^{-1} after 50 repetitive cycles and it showed good rate capability as well. The SnO_2 HS were also found to

be strongly fluorescent, thereby suggesting their potential for energy harvesting applications in addition to electrochemical energy storage.

Acknowledgements
We acknowledge ARCI for financial assistance and TEM characterization.

Authors Affiliations
[a] *Akkisetty Bhaskar, Department of Materials Science and Metallurgical Engineering,*
[b,*] *Melepurath. Deepa, Department of Chemistry,*
[a,b] *Indian Institute of Technology Hyderabad, Ordnance Factory Estate, Yeddumailram,-502205, Andhra Pradesh, India. Tel: +91-40-23016024, Fax: +91-40-23016003, E-mail: mdeepa@iith.ac.in*
[c] *T. N. Rao, Nanocenter, ARCI, Hyderabad, India.*

†Electronic Supplementary Information (ESI) available: XRD patterns and FE-SEM image of SnO_2 HS.

References
1. Z. Wang, L. Zhou and X. W. Lou, *Adv. Mater.* 2012, **24**, 1903-1911.
2. H. B. Wu, J. S. Jun Song Chen, H. H. Hng and X. W. Lou, *Nanoscale*, 2012, **4**, 2526-2542.
3. F. Gyger, M. Hübner, C. Feldmann, N. Barsan and U. Weimar, *Chem. Mater.*, 2010, **22**, 4821-4827
4. J. Qian, P. Liu, Y. Xiao, Y. Jiang, Y. Cao, X. Ai and H. Yang, Adv. Mater., 2009, **21,** 3663-3667.
5. X. Lai, J. E. Halpert and D. Wang, *Energ. Environ. Sci.*, 2012, **5**, 5604-5618.
6. M. V. Reddy, G. V. Subba Rao and B. V. R. Chowdari, *Chem. Rev.*, 2013, **113,** 5364-5457.
7. A. Bhaskar, M. Deepa and T. N. Rao, *ACS Appl. Mater. Interfaces*, 2013, **5**, 2555-2566.
8. P. Poizot, S. Laruelle, S. Grugeon, L. Dupont and J-M. Tarascon, *Nature*, 2000, **407**, 496-499.
9. P. L. Taberna, S. Mitra P. Poizot, P. Simon and J. M. Tarascon, *Nat. Mater.*, 2006, **5**, 567-573.
10. D. Deng, M. G. Kim, J. Y. Lee and J. Cho, *Energ. Environ. Sci.*, 2009, **2**, 818-837.
11. J. S. Chen and X. W. Lou, *Small*, 2013, **9**, 1877-1893.
12. J. Y. Huang, L. Zhong, C. M. Wang, J. P. Sullivan, W. Xu, L. Q. Zhang, S. X. Mao, N. S. Hudak, X. H. Liu, A. Subramanian, H. Fan, L. Qi, A. Kushima and J. Li, *Science*, 2010, **330**, 1515-1520.
13. R. A. Huggins, *Solid State Ionics*, 1998, **113**, 57-67.
14. D. Aurbach, A. Nimberger, B. Markovsky, E. Levi, E. Sominski and A. Gedanken, *Chem. Mater.*, 2002, **14**, 4155-4163.
15. K. Kravchyk, L. Protesescu, M. I. Bodnarchuk, F. Krumeich, M. Yarema, M. Walter, C. Guntlin and M. V. Kovalenko, *J. Am. Chem. Soc*. 2013, **135**, 4199-4202.
16. Y. Chen, J. Ma, Q. Li and T. Wang, *Nanoscale*, 2013, **5**, 3262-3265.
17. C. Kim, M. Noh, M. Choi, J. Cho and B. Park, *Chem. Mater.*, 2005, **17**, 3297-3301.
18. A. Bhaskar, M. Deepa, M. Ramakrishna and T. N. Rao, *J. Phys. Chem. C*, 2014, **118**, 7296-7306.
19. S. Ding, X. W. Lou, *Nanoscale*, 2011, **3**, 3586-3588.
20. H. X. Yang, J. F. Qian, Z. X. Chen, X. P. Ai and Y. L. Cao, *J. Phys. Chem. C*, 2007, **111**, 14067-14071.
21. Y. J. Hong, M. Y. Son and Y. C. Kang, *Adv. Mater.*, 2013, **25**, 2279-2283.
22. X. W. Lou, Y. Wang, C. Yuan, J. Y. Lee and L. A. Archer, *Adv. Mater.*, 2006, **18**, 2325-2329.
23. H. Wang, F. Fu, F. Zhang, H. E. Wang, S. V. Kershaw, J. Xu, S. G. Sunb and A. L. Rogach, *J. Mater. Chem.*, 2012, **22**, 2140-2148.
24. W. S. Kim, Y. Hwa, J. H. Jeun, H. J. Sohn and S. H. Hong, *J. Power Sources*, 2013, **225**, 108-112.
25. Y. Chen, Q. Z. Huang, J. Wang, Q. Wang and J. M. Xue, *J. Mater. Chem.*, 2011, **21**, 17448-17453.
26. X. W. Lou, C. M. Li and L. A. Archer, *Adv. Mater.* 2009, **21**, 2536-2539.
27. F. Caruso, R. A. Caruso and H. Mohwald, *Science*, 1998, *282*, 1111-1114.
28. Y. Wang, J. Y. Lee and H. C. Zeng, *Chem. Mater.*, 2005, **17**, 3899-3903.
29. X. Xu, J. Liang, H. Zhou, D. Lv, F. Liang, Z. Yang, S. Ding and D. Yu, *J. Mater. Chem. A.*, 2013, **1**, 2995-2998.
30. J. Wang, N. Du, H. Zhang, J. Yu. and D. Yang, *J. Phys. Chem. C*, 2011, **115**, 11302-11305.
31. H. Wang, Q. Liang, W. Wang, Y. An, J. Li and L. Guo, *Cryst. Growth Des.*, 2011, **11**, 2942-2947.
32. H. B. Wu, J. S. Chen, X. W. Lou and H. H. Hng, *J. Phys. Chem. C*, 2011, **115**, 24605-24610.
33. J. Liu, Y. Li, X. Huang, R. Ding, Y. Hu, J. Jianga and L. Liao, *J. Mater. Chem.*, 2009, **19**, 1859-1864.
34. M. S. Park, G. X. Wang, Y. M. Kang, D. Wexler, S. X. Dou and H. K. Liu, *Angew. Chem. Int. Ed.*, 2007, **46**, 750-753.
35. X. Wang, Z. Li,Q. Li, C. Wang, A. Chen, Z. Zhang, R. Fan and L. Yin, *Cryst Eng Comm*., 2013, **15**, 3696-3704.
36. R. L. Penn and J. F. Banfield, *Science*, 1998, **281**, 969-971.
37. C. Wang, G. Du, K. Ståhl, H. Huang, Y. Zhong and J. Z. Jiang, *J. Phys. Chem. C*, 2012, **116**, 4000-4011.
38. Y. Yin, R. M. Rioux, C. K. Erdonmez, S. Hughes, G. A. Somorjai and A. P. Alivisatos, *Science*. 2004, **304**, 711-714.
39. W. Wang, M. Dahl and Y. Yin, *Chem.Mater.*, 2013, **25**, 1179-1189
40. S. Luo, J. Fan, W. Liu, M. Zhang, Z. Song, C. Lin, X. Wu and P. K. Chu, *Nanotechnology*, 2006, **17**, 1695-1699
41. Y. C. Her, J. Y. Wu, Y. R. Lin and S. Y. Tsai, *Appl. Phys. Lett.*, 2006, **89**, 043115-3.
42. Y. Wang, M. Guo, M. Zhang and X. Wang, *Scripta Materialia*, 2009, **61**, 234-236.
43. V. Briois, S. Belin, M. Z. Chalaca, R. H. A. Santos, C. V. Santilli and S. H. Pulcinelli, *Chem. Mater.*, 2004, **16**, 3885-3894.
44. Y. Cui, G. Wang and D. Pan, *J. Mater. Chem.*, 2012, **22**, 12471-12473.
45. I. Robel, V. Subramanian, M. Kuno, and P. V. Kamat, *J. Am. Chem. Soc.*, 2006, **128**, 2385-2393.

46. Y. F. Zhukovskii, E. A. Kotomin, P. Balaya and J. Maier, *Solid State Sci.*, 2008, **10,** 491-495.

Figures

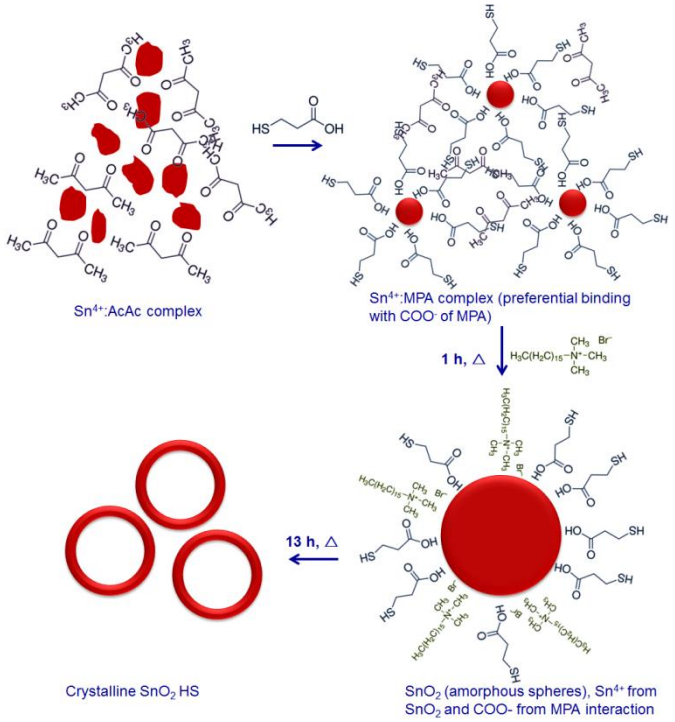

Scheme 1. Formation of discrete SnO_2 HS from a solution containing Sn^{2+} salt, MPA, AcAc and CTAB.

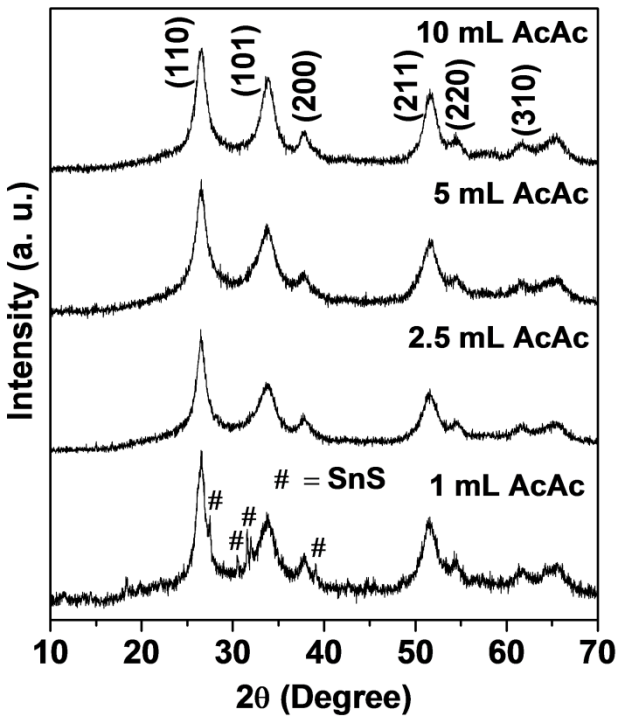

Figure 1. Powder XRD patterns of SnO_2 samples synthesized from precursor solutions containing 1, 2.5, 5 and 10 mL of AcAc. Each solution also contained 3.324 mmol of $SnCl_2.2H_2O$, 1.1 g of MPA, 100 mg of CTAB and each solution was heated hydrothermally for 13 h at 160 °C.

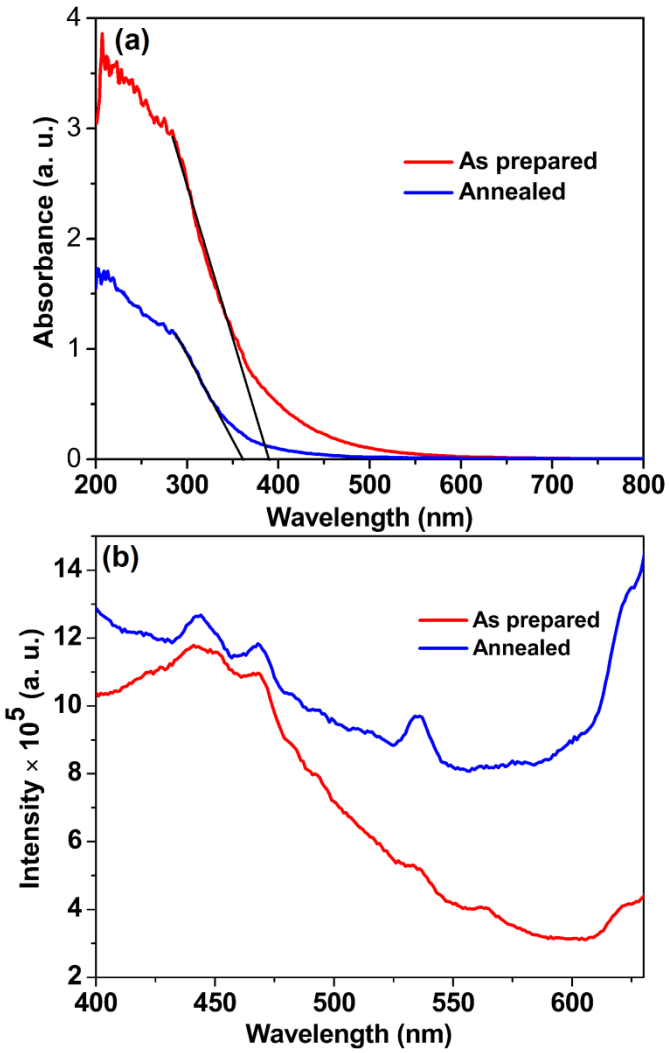

Figure 2. (a) UV-vis diffuse reflectance spectra of as-prepared and annealed (at 500 °C for 3 h) SnO_2 HS and (b) room temperature PL emission spectra of as-prepared and annealed (at 500 °C for 3 h) SnO_2 HS. The SnO_2 HS were prepared from a solution with 3.324 mmol of $SnCl_2.2H_2O$, 5 mL AcAc, 1.1 g of MPA, 100 mg of CTAB and the solution was heated hydrothermally for 13 h at 160 °C.

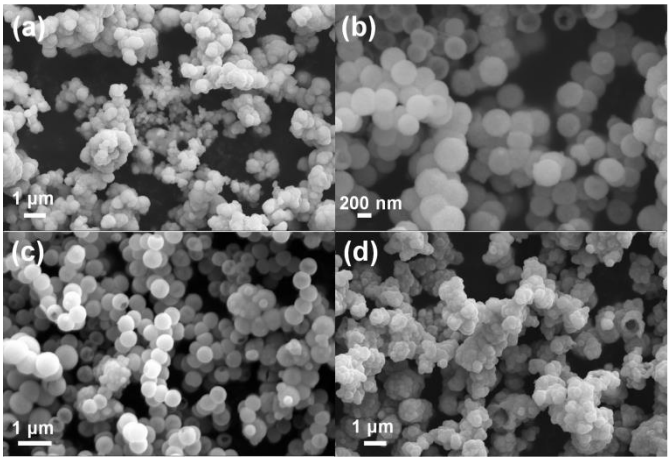

Figure 3. FESEM images of SnO_2 samples synthesized from precursor solutions containing (a) 1, (b) 2.5, (c) 5 and (d) 10 mL of AcAc. Each solution also contained 3.324 mmol of $SnCl_2.2H_2O$, 1.1 g of MPA, 100 mg of CTAB and each solution was heated hydrothermally for 13 h at 160 °C.

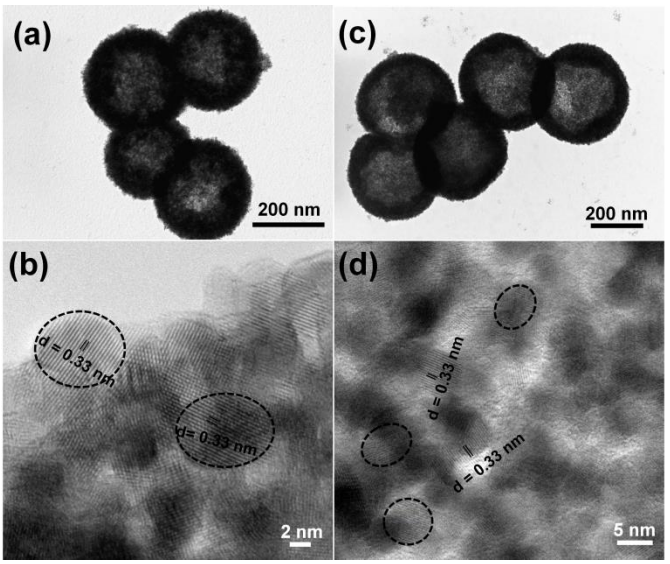

Figure 4. TEM images of SnO_2 HS obtained from solutions containing (a) 2.5 mL of AcAc, (b) corresponding lattice scale image, (c) 5 mL of AcAc and (d) corresponding lattice scale image. Each solution also contained 3.324 mmol of $SnCl_2.2H_2O$, 1.1 g of MPA, 100 mg of CTAB and was heated hydrothermally for 13 h at 160 °C.

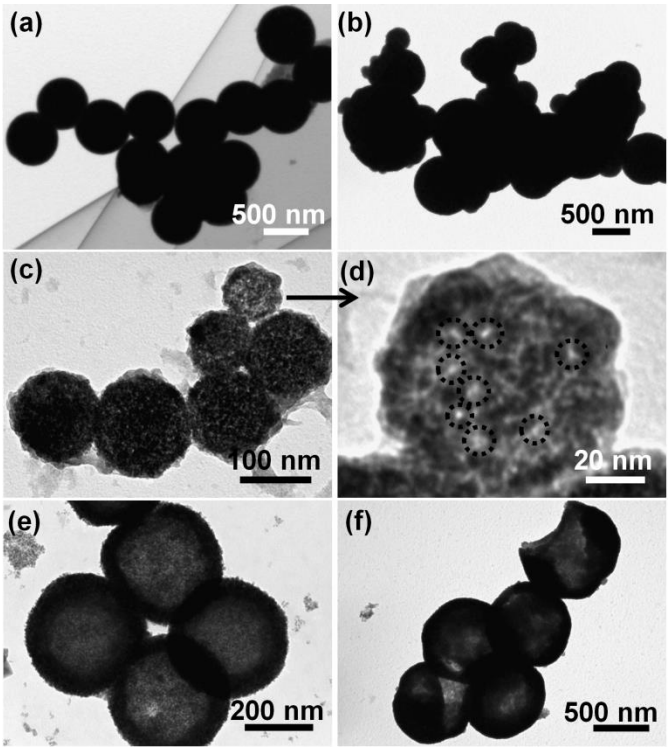

Figure 5. TEM images of the samples obtained after hydrothermally heating the precursor solution containing 3.3 mmol of $SnCl_2.2H_2O$, 5 mL of AcAc, 1.1 g of MPA and 100 mg CTAB for intervals of (a) 1, (b) 4, (c, d) 10, (e) 13 and (f) 24 h at a constant temperature of 160 °C.

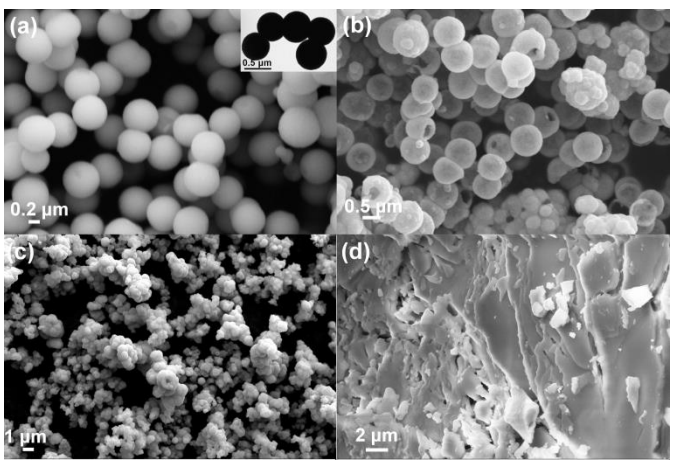

Figure 6. FESEM images of SnO_2 powders obtained after hydrothermal heating at (a) 140 and (b) 180 °C for 13 h. The solutions contained 3.3 mmol of $SnCl_2.2H_2O$, 5 mL of AcAc, 1.1 g of MPA and 100 mg of CTAB. (c) SnO_2 prepared from a solution containing 3.3 mmol of $SnCl_2.2H_2O$, 5 ml of AcAc and 1.1 g of MPA (no CTAB) and (d) SnO_2 prepared from a solution containing 3.3 mmol of $SnCl_2.2H_2O$, 5 ml of AcAc and 100 mg of CTAB (no MPA). In (c) and (d) the samples were heated at 160 °C for 13 h (under hydrothermal conditions).

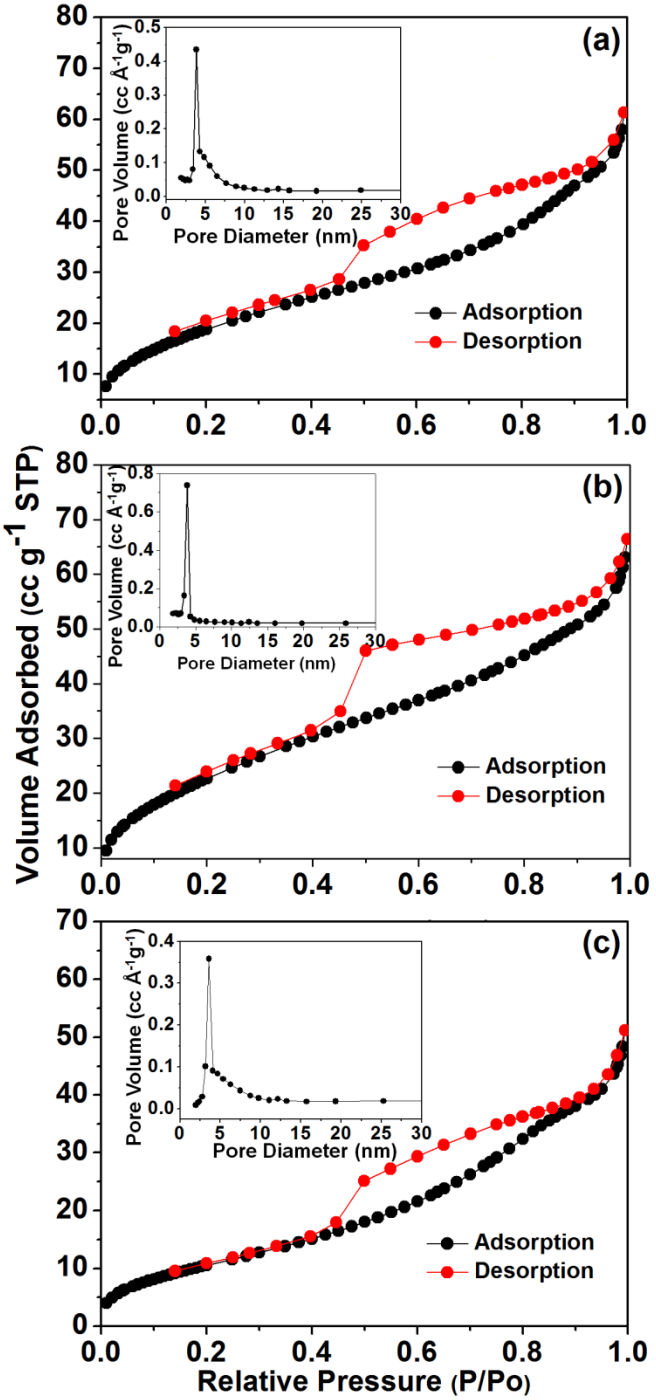

Figure 7. N_2 adsorption-desorption isotherm curves at 77 K for (a) 200 (b) 350 and (c) 750 nm SnO_2 HS obtained by BET analysis, and the curves in the insets depict the corresponding pore-size distribution based on the BJH method during desorption.

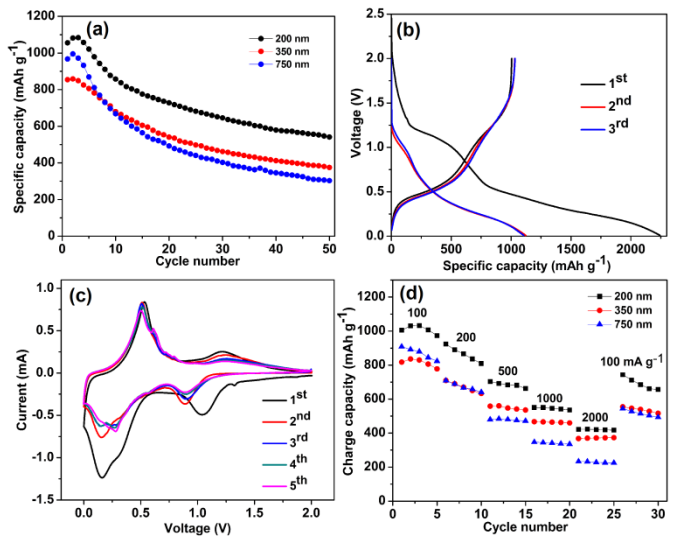

Figure 8. (a) Cycling performance of SnO_2 HS of 200, 350 and 750 nm dimensions at a current density of 100 mA g^{-1}, (b) discharge-charge curves for the first three cycles, (c) cyclic voltammograms recorded at a scan rate of 0.1 mV s^{-1} *versus* Li, for the first five cycles for 200 nm SnO_2 HS and (d) the rate performance of SnO_2 HS of 200, 350 and 750 nm.

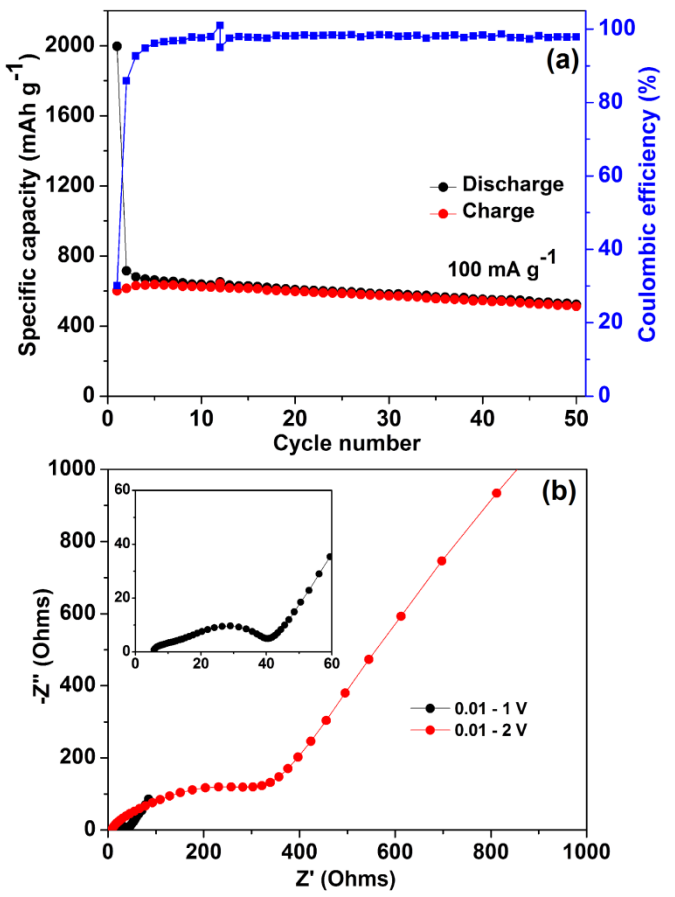

Figure 9. (a) Cycling performance and Coulombic efficiency of 200 nm size SnO_2 HS at 100 mA g^{-1} current density between 0.01-1 V *versus* Li and (b) Nyquist plots after 50 cycles of 200 nm SnO_2 HS over two different potential ranges.

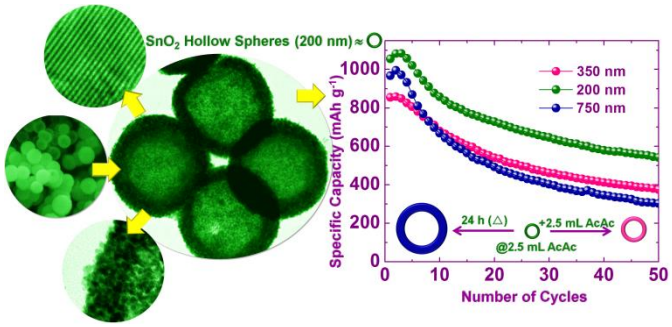

Graphical Abstract

Excellent control over SnO_2 hollow sphere size leads to outstanding capacity performance and retention with cycling.